ARTICLE

Probing the Electronic Structure of the CoB_{16}^- Drum Complex: Unusual Oxidation State of Co^{-1}†

Wan-Lu Li[a‡], Teng-Teng Chen[b‡], Zhi-Yu Jiang[a], Wei-Jia Chen[b], Han-Shi Hu[a], Lai-Sheng Wang[b*], Jun Li[a*]

a. Department of Chemistry, Key Laboratory of Organic Optoelectronics & Molecular Engineering of Ministry of Education, Tsinghua University, Beijing 100084, China
b. Department of Chemistry, Brown University, Providence, Rhode Island 02912, USA

(Dated: Received on March 17, 2019; Accepted on March 31, 2019)

Since the discovery of the first drum-like CoB_{16}^- complex, metal-doped drum-like boron nanotubular structures have been investigated with various metal dopants and different tubular size, forming a new class of novel nanostructures. The CoB_{16}^- cluster was found to be composed of a central Co atom coordinated by two fused B_8 rings in a tubular structure, representing the potential embryo of metal-filled boron nanotubes and providing opportunities to design one-dimensional metal-boron nanostructures. Here we report improved photoelectron spectroscopy and a more in-depth electronic structure analysis of CoB_{16}^-, providing further insight into the chemical bonding and stability of the drum-like doped boron tubular structures. Most interestingly, we find that the central Co atom has an unusually low oxidation state of -1 and neutral CoB_{16} can be viewed as a charge transfer complex ($Co^-@B_{16}^+$), suggesting both covalent and electrostatic interactions between the dopant and the boron drum.

Key words: Photoelectron spectroscopy, Metal-boron clusters, *Ab initio* calculations, Chemical bonding

I. INTRODUCTION

Boron forms a wide variety of bulk boride materials, such as the superconductor MgB_2, superhard material ReB_2 and boron arsenide crystals with ultra-high thermal conductivity [1–5]. Investigations on nanoclusters of borides can provide insight about how the interesting properties of the bulk materials emerge as a function of size and provide fundamental knowledge to design materials with new properties. In the past two decades, extensive experimental studies in combination with quantum chemistry calculations have been devoted to size-selected boron clusters [6–9], giving rise to the discoveries of novel nanostructures, such as borophenes, borospherenes, and tubular nanostructures [10–14].

Doping boron clusters with a single metal atom can give rise to the simplest boride clusters, which allow one to study at the most detailed level how metal atoms interact with boron. Joint photoelectron spectroscopy (PES) experiments and *ab initio* calculations have shown that for small mono-transition metal doped boron clusters, perfect molecular wheels are formed ($M©B_n^-$, n=8−10), which obey an electronic design principle based on σ and π double aromaticity [15–19]. For larger mono-metal doped boron clusters, half-sandwich-like nanotubular and planar structures have been found [20–26]. For boron clusters doped by two lanthanide atoms, inverse sandwich structures with unique delocalized δ-bonding have been observed [27, 28]. Among the mono-transition metal doped clusters, CoB_{16}^- was the first drum-like tubular nanocluster observed to have a very high coordination number [21], which was selected as one of the "Molecules of the Year" in 2015 by Chem. Eng. News [29]. Shortly afterward, $M_nB_{16}^-$ became the second doped-boron cluster found to possess a similar drum structure [24].

Because of its complicated PE spectra and electronic structure, only the first two detachment channels were computed and compared with the experiment for the two low-lying isomers (D_{8d} and C_{4v}) of CoB_{16}^- in the previous study [21]. Here we report improved photoelectron spectrum for CoB_{16}^- and more detailed quantum chemical calculations. All detachment channels in the energy range of the experimental spectrum are calculated to yield simulated spectra. Using the ΔSCF-TDDFT approach with the SAOP model, we show in the present study that the simulated spectra agree well with the experimental data. The bonding between the Co atom and the B_{16} tube is further analyzed using different chemical bonding methods. Interestingly, both molecular orbital (MO) and charge analyses reveal that

†Part of the special issue for "the 19th International Symposium on Small Particles and Inorganic Clusters"
‡These authors contributed equally to this work.
*Authors to whom correspondence should be addressed. E-mail: Lai-Sheng_Wang@brown.edu, junli@tsinghua.edu.cn

the extra charge in CoB_{16}^- is localized on the metal atom, resulting in a rare −1 oxidation state for Co.

II. METHODS

A. Experimental methods

The experiment was carried out by a magnetic-bottle PES apparatus equipped with a laser vaporization cluster source, details of which can be found elsewhere [9, 30]. Briefly, the CoB_{16}^- clusters were produced by laser vaporization of a hot-pressed disk target made from a mixed powder consisting of Co and isotopically-enriched ^{11}B. The nascent clusters were thermalized in a large waiting room nozzle and cooled in a supersonic expansion by a He carrier gas seeded with 5% Ar. Anionic clusters were extracted and analyzed by a time-of-flight mass spectrometer. The CoB_{16}^- clusters of interest were selected by a mass gate and decelerated before being photodetached by the 193 nm (6.424 eV) radiation from an ArF excimer laser. Photoelectrons were collected and analyzed by a 3.5 m long magnetic-bottle analyzer at nearly 100% efficiency. The resolution of the apparatus is about 2.5%, that is, around 25 meV for 1 eV electrons. Compared to the previous study [21], the signal-to-noise ratios are significantly improved due to the newly installed "funnel-type" microchannel plates (MCP) electron detector, which has a 30% increase in the electron detection efficiency [31].

B. Computational methods

Extensive global minimum searches were done previously for CoB_{16}^- at different levels of theory and for the lowest three isomers at the high level of RO-CCSD(T) [21]. Two nearly degenerate drum-like structures isomer I (D_{8d}, $^3A_2$) and isomer II (C_{4v}, $^1A_1$) were found to compete for the global minimum in the previous study. We reexamined the relative energies of the fully optimized isomers I and II at the M06-2X/TZP level [32] with the cc-pVTZ basis sets [33] for B, and the ECP10MDF pseudopotential and the corresponding valence basis set for Co [34, 35]. The first vertical detachment energies (VDE) of the two isomers were computed accurately at the ROCCSD(T) level in the previous study. In the present study, we did not compute the first VDE and instead focused on the higher VDEs which were calculated using the ΔSCF-TDDFT formalism [36] in conjunction with the SAOP model [37], as implemented in the ADF 2013.01 software [38]. In these calculations, we used the triple-ζ Slater type basis sets plus one polarization function (TZP) [39] and the ZORA approximation [40] to account for the scalar relativistic effect. The computed VDEs were used to generate simulated spectra by fitting each VDE with a unit-area Gaussian function of 0.15 eV width. To gain further insight into the chemical bonding and stability of the drum structures, we performed canonical molecular orbital (CMO) and energy decomposition analyses (EDA) combined with the natural orbitals for chemical valence (NOCV) theory [41–43], with the GGA-PBE functional [44].

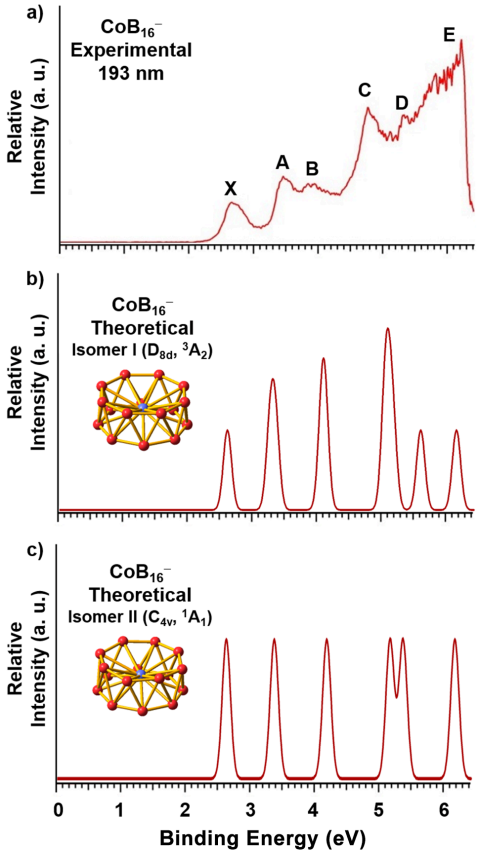

FIG. 1 Photoelectron spectra of CoB_{16}^- at 193 nm (6.424 eV) (a) compared with the simulated spectra for isomers I (b) and II (c) at the TDDFT-SAOP/TZP level.

III. RESULTS AND DISCUSSION

A. Comparison between experimental and theoretical results

The new PE spectrum of CoB_{16}^- at 193 nm is presented in FIG. 1(a). The spectral features are similar to those reported in the previous study [21], except that the signal-to-noise ratios are improved, in particular in the high binding energy side [24]. The VDEs measured in the current study given in Table I are consistent with those reported in the previous study. The computed VDEs for isomers I and II are compared with the experimental data in Table I, where the first VDEs are from the previous ROCCSD(T) calculations.

Before presenting the computed VDEs, let us first understand the relationship between the structures of isomer I (D_{8d}) and isomer II (C_{4v}), as illustrated by the energy level correlation diagram in FIG. 2. Isomer I was

DOI:10.1063/1674-0068/cjcp1903050

TABLE I Experimental and theoretical VDEs of CoB_{16}^- at the TD-SAOP/TZP level with D_4 symmetry, which is the smallest subgroup of D_{8d}. The VDE1 values are obtained from the ROCCSD(T)/Def2-TZVP calculations [21].

Obs. features	VDE/eV (Exp.)	Final state and electronic configuration	VDE/eV (Calc.)
X	2.68(6)	Isomer I: $(^2E_2)\ldots 3e_1^4 1e_5^4 2e_2^4 4e_1^4 2e_7^4 5a_1^2 3b_2^2 \mathbf{3e_2^1}$	2.59
		Isomer II: $(^2B_1)\ldots 3b_2^2 6e^4 7e^4 8e^4 8a_1^2 9a_1^2 \mathbf{4b_1^1}$	2.61
A	3.47(4)	Isomer I: $(^4B_2)\ldots 3e_1^4 1e_5^4 2e_2^4 4e_1^4 2e_7^4 5a_1^2 \mathbf{3b_2^1} 3e_2^2$	3.25
		Isomer I: $(^2B_2)\ldots 3e_1^4 1e_5^4 2e_2^4 4e_1^4 2e_7^4 5a_1^2 \mathbf{3b_2^1} 3e_2^2$	3.33
		Isomer II: $(^2A_1)\ldots 3b_2^2 6e^4 7e^4 8e^4 8a_1^2 \mathbf{9a_1^1} 4b_1^2$	3.35
B	3.95(5)	Isomer I: $(^2A_1)\ldots 3e_1^4 1e_5^4 2e_2^4 4e_1^4 2e_7^4 \mathbf{5a_1^1} 3b_2^2 3e_2^2$	4.05
		Isomer I: $(^4A_1)\ldots 3e_1^4 1e_5^4 2e_2^4 4e_1^4 2e_7^4 \mathbf{5a_1^1} 3b_2^2 3e_2^2$	4.09
		Isomer II: $(^2A_1)\ldots 3b_2^2 6e^4 7e^4 8e^4 \mathbf{8a_1^1} 9a_1^2 4b_1^2$	4.16
C	4.78(4)	Isomer I: $(^2E_7)\ldots 3e_1^4 1e_5^4 2e_2^4 4e_1^4 \mathbf{2e_7^3} 5a_1^2 3b_2^2 3e_2^2$	5.02
		Isomer I: $(^4E_7)\ldots 3e_1^4 1e_5^4 2e_2^4 4e_1^4 \mathbf{2e_7^3} 5a_1^2 3b_2^2 3e_2^2$	5.06
		Isomer I: $(^4E_1)\ldots 3e_1^4 1e_5^4 2e_2^4 \mathbf{4e_1^3} 2e_7^4 5a^2 3b_2^2 3e_2^2$	5.14
		Isomer II: $(^2E)\ldots 3b_2^2 6e^4 7e^4 \mathbf{8e^3} 8a_1^2 9a_1^2 4b_1^2$	5.14
D	5.34(5)	Isomer II: $(^2E)\ldots 3b_2^2 6e^4 \mathbf{7e^3} 8e^4 8a_1^2 9a_1^2 4b_1^2$	5.34
E−F	5.8−6.2	Isomer I: $(^2E_1)\ldots 3e_1^4 1e_5^4 2e_2^4 \mathbf{4e_1^3} 2e_7^4 5a_1^2 3b_2^2 3e_2^2$	5.57
		Isomer I: $(^2E_2)\ldots 3e_1^4 1e_5^4 \mathbf{2e_2^3} 4e_1^4 2e_7^4 5a_1^2 3b_2^2 3e_2^2$	6.12
		Isomer II: $(^2E)\ldots 3b_2^2 \mathbf{6e^3} 7e^4 8e^4 8a_1^2 9a_1^2 4b_1^2$	6.14

Note: the orbitals in bold face indicate the major electron detachment channels.

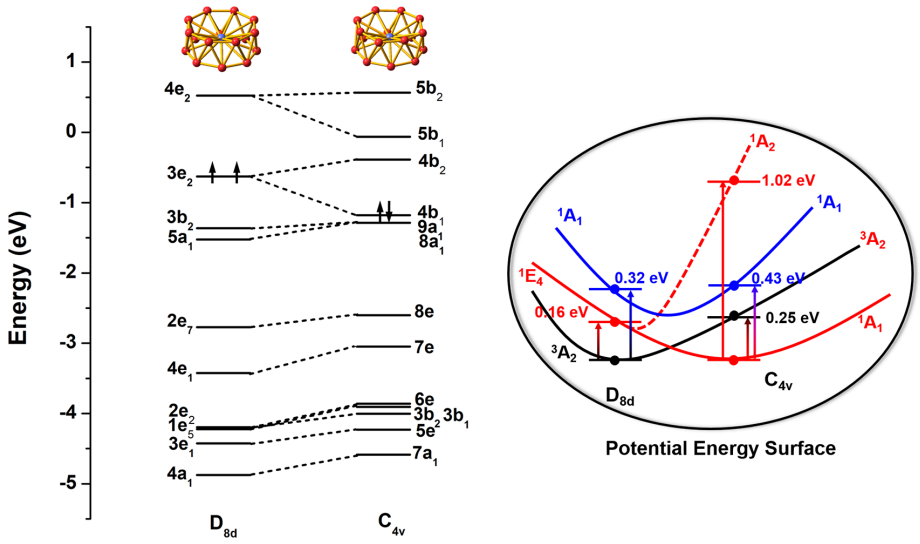

FIG. 2 Energy level correlation diagram between isomer I (D_{8d}, $^3A_2$) and isomer II (C_{4v}, $^1A_1$) of CoB_{16}^-. The right panel shows the schematic potential energy surfaces of the $^3A_2$, $^1E_4$, and $^1A_1$ electronic states along the distortion coordinate to C_{4v}. The excitation energies shown in the inset were estimated using TDDFT with the SAOP functional.

found to have a triplet ground state ($^3A_2$) with two unpaired electrons in the $3e_2$ doubly degenerate HOMO. The $3e_2^2$ configuration can give rise to three electronic states in D_{8d} symmetry, $^3A_2+^1A_1+^1E_4$. The relative energies of the three states and their potential energy surfaces are depicted schematically in the right panel of FIG. 2. The $^3A_2$ term is the ground state and the $^1E_4$ term is the first excited state with a 0.16 eV excitation energy at the D_{8d} symmetry, while the $^1A_1$ term is the second excited state with an excitation energy of 0.32 eV. Upon optimization, the $^1E_4$ state distorts to C_{4v} symmetry due to the Jahn-Teller effect and splits into two states $^1A_2$ and $^1A_1$ (Table II) with a large energy difference. The $^1A_1$ state is found to be significantly stabilized under C_{4v} symmetry and becomes the ground state of isomer II. The C_{4v} isomer II features alternating short-long B−B bond lengths in the B_8 ring, in contrast to the D_{8d} isomer I that has equal B−B bond lengths. At the M06-2X/TZP level of theory, the $^1A_1$ ground state of the C_{4v} isomer II is more

DOI:10.1063/1674-0068/cjcp1903050

TABLE II Reduction of species from the D_{8d} point group to those of the D_4 and C_{4v} point groups.

D_{8d}	D_4	C_{4v}	χ
A_1	A_1	A_1	z^2
A_2	A_2	A_2	
B_1	A_1	A_2	
B_2	A_2	A_1	
E_1	E	E	
E_2	B_1+B_2	B_1+B_2	xy, x^2-y^2
E_3	E	E	
E_4	A_1+A_2	A_1+A_2	
E_5	E	E	
E_6	B_1+B_2	B_1+B_2	
E_7	E	E	xz, yz

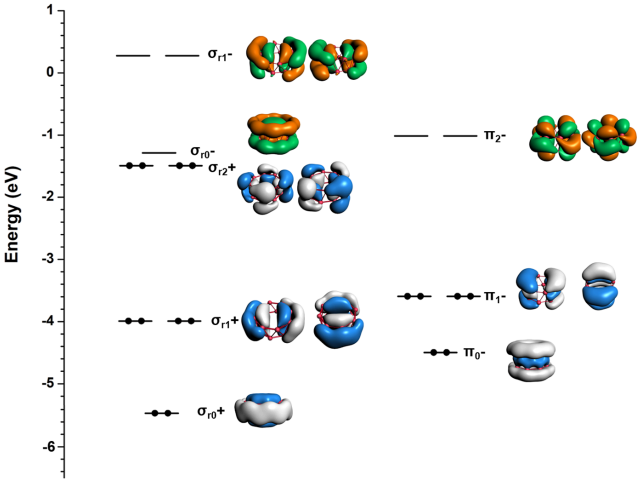

FIG. 3 A local coordinate system (LCS) analysis for the B_{16} tube at the theoretical level of PBE/TZP. Here, r in σ_r represents the radial direction of each B_8 ring, the value in the subscript corresponds to the number of the orbital node, the "+" and "−" signs represent positive and negative overlaps, respectively.

stable than the $^3A_2$ state of isomer I by 2.50 kcal/mol, in good agreement with the 1.4 kcal/mol energy difference at the ROCCSD(T) level reported previously [21]. Hence, both isomers are expected to be present experimentally and have to be considered in the interpretation of the observed PE spectrum.

The ΔSCF-TDDFT method combined with the SAOP functional has been found to be an effective approach to simulate PE spectra of transition-metal doped boron clusters [22–25]. The calculated higher VDEs for isomers I and II of CoB_{16}^- using this approach are compared with the experimental data in Table I. The simulated spectra are compared with the observed spectrum in FIG. 1 (b) and (c). The simulated spectra resemble each other due to the similarities in the geometrical and electronic structures of the two isomers. Table I also lists the detailed electronic configurations and the final states of individual detachment channels. In the previous study [21], only the first two detachment channels were computed and compared with the experimental values. The good agreement between the fully simulated spectra of the isomers I/II and the experimental data confirm the previous study and provide further evidence for the co-existence of the two drum isomers for CoB_{16}^-.

B. Chemical bonding analyses

In order to gain further insight into the chemical bonding of the CoB_{16}^- drum structure, we first investigate the bonding in the B_{16} tube in the local coordinate system (LCS) as shown in FIG. 3, where the radial orbitals (σ_r) point to the B_8 ring center and the orthogonal tangential orbitals (π) lie along the C_8 axis. We only consider the frontier orbitals in FIG. 3 and classify them into two groups, σ_r and π. The σ type radial orbitals on the B_{16} tube mainly interact with the central atom Co (see discussion below), because of the more efficient overlap with the 3d orbitals. However, these orbitals are already fully occupied and cannot accept extra electrons from the central metal atom.

The detailed CMO analysis for isomer I (D_{8d}, $^3A_2$) is shown in FIG. 4. It is seen that the Co 3d orbitals are transformed into $a_1+e_2+e_7$ upon coordination by the B_{16} tube ligand. The half-filled $3e_2$ HOMO is composed mainly of 2p π bonding orbitals between the two B_8 rings. The $3b_2$ HOMO−1 consists of σ bonding along the periphery of each B_8 ring, whereas the $5a_1$ HOMO−2 is predominantly from the Co $3d_{z^2}$ orbital. The central Co atom interacts with the B_{16} tube via its $3d_{xz}/3d_{yz}$ and $3d_{xy}/3d_{x^2-y^2}$ orbitals to form the $2e_7$ and $2e_2$ MOs, respectively. The remaining MOs are all primarily from the B sp orbitals. It is interesting to note the qualitative agreement between the MO energy levels in FIG. 4 and the overall spectral pattern observed for CoB_{16}^- (FIG. 1(a)), as shown more quantitatively in Table I. The CMOs of isomer II (C_{4v}, $^1A_1$) are similar to those of isomer I, because of the relatively minor distortion from the D_{8d} symmetry.

The MO analysis shown in FIG. 4 suggests that the bonding in CoB_{16}^- can be depicted as $Co^-@B_{16}$, that is, the extra charge seems to be localized on the Co center, resulting in an unexpected −1 oxidation state (OS) for Co. The atomic orbital percentages of the Co 3d orbitals for each bonding MO are given in FIG. 4 and highlighted in red. Due to the large repulsion effect with the B_{16} tube ligand, the Co 4s electrons are promoted to the Co 3d orbitals in the CoB_{16}^- complex. In the B_{16} framework, the antibonding $2e_2$ orbitals (*i.e.*, σ_{r2}^+ in FIG. 3) lie higher in energy than the Co 3d orbitals, and are significantly destabilized upon interaction with the Co $3d_{xy}/3d_{x^2-y^2}$ orbitals via an inverted ligand field interaction [45]. As a result, the Co $3d_{xy}/3d_{x^2-y^2}$ or-

DOI:10.1063/1674-0068/cjcp1903050

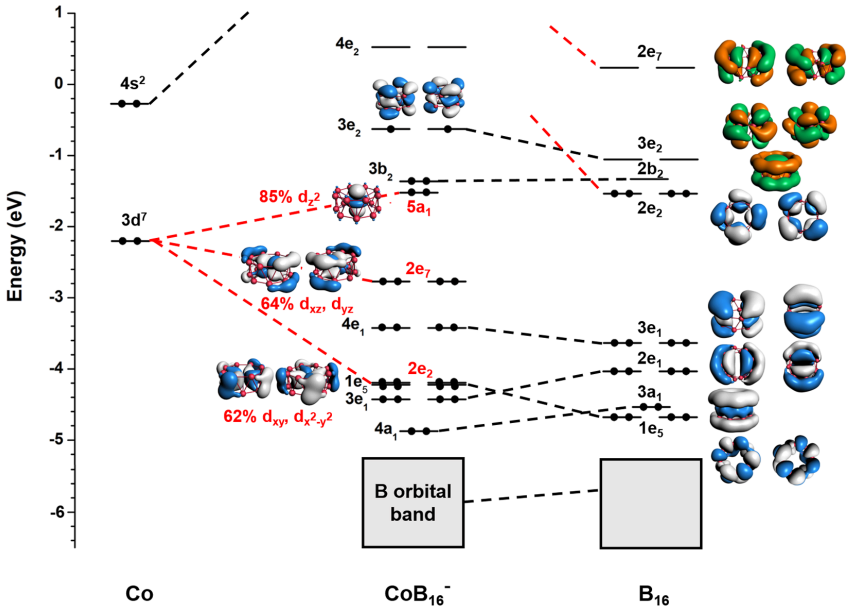

FIG. 4 The MO diagram for the D_{8d} ($^3A_2$) isomer of CoB_{16}^- at the PBE/TZP level. The $3e_2$ orbital is the SOMO with two unpaired electrons and the $4e_2$ orbital is the LUMO. Bonding orbitals between Co and B_{16} are shown in red.

TABLE III Energy decomposition analyses of CoB_{16}^- at the PBE/TZP level using the Co^- (d^{10}) and B_{16} ($\ldots 3e_1{}^4 2e_2{}^0 2b_2{}^2 3e_2{}^2$) fragments. Energy values are given in kcal/mol.

$\Delta E_{\rm Pauli}$	$\Delta E_{\rm elstat}$	$\Delta E_{\rm orb}$*					$\Delta E_{\rm int}$
		$\Delta E_{1\alpha}$	$\Delta E_{2\alpha}$	$\Delta E_{1\beta}$	$\Delta E_{2\beta}$	$\Delta E_{\rm rest}$	
395.60	−410.19	−104.4	−90.4	−104.8	−90.6	−58.3	−463.13
		(23.3%)	(20.1%)	(23.4%)	(20.2%)	(13.0%)	

* The values in the parentheses correspond to the contribution percentage to the total orbital interaction.

bitals are stabilized and the four electrons on the antibonding $2e_2$ orbitals were promoted to the B_{16} $2b_2$ (fully occupied) and $3e_2$ (half-filled) orbitals. Hence, upon coordination to Co, the B_{16} tube experiences no electron gain or loss, while Co accepts the extra electron in the CoB_{16}^- anion, resulting in an oxidation state of −1 for Co. Indeed the charge population indices of the Co atom from the Mulliken [45] and MDC-q [46] approaches, calculated to be −0.12 and −0.99 e, agree with the unusual −1 OS for Co. This Co^{-1} OS is unusual, and it is consistent with the fact that boron has higher atomic orbital energies (cf. FIG. 3 of Ref.[14]), leading to unusually low oxidation-state metal centers in boron-metal complexes [26, 48]. It is also interesting to note that neutral CoB_{16} upon electron detachment from the $3e_2$ HOMO can be viewed as a charge transfer complex, $Co^-@B_{16}^+$, with additional ionic bonding and enhanced stability.

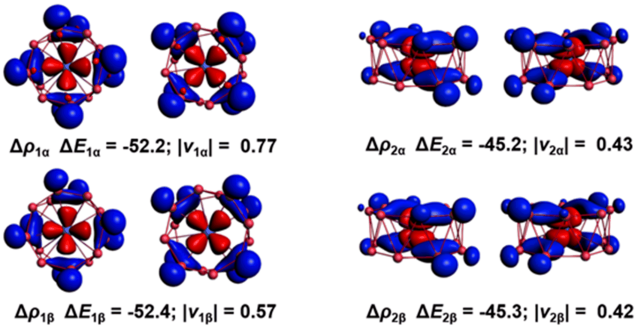

FIG. 5 Plot of deformation densities $\Delta\rho_1$ and $\Delta\rho_2$ (isosurface value=0.002 a.u.) of the orbital interactions between the central Co and the B_{16} frame for both α and β electrons. ΔE_n and $|\nu_n|$ are the interaction energies (in kcal/mol) and charge eigenvalues (in e) for each degenerate orbital, where the charge flow direction is from red to blue (red and blue represent charge depletion and accumulation, respectively.).

C. Energy decomposition analyses

The nature of the $Co^{-1}\ldots B_{16}$ interaction in the D_{8d} CoB_{16}^- drum is further investigated by unrestricted EDA-NOCV analyses, which reveal detailed contributions of each bonding interaction, as summarized in Table III. For each spin, the breakdown of the total orbital term into pairwise contributions includes two ma-

DOI:10.1063/1674-0068/cjcp1903050

jor contributions $\Delta E_{1\alpha/\beta}$ and $\Delta E_{2\alpha/\beta}$, which can be visually identified with the associated deformation densities $\Delta\rho_{1\alpha/\beta}$ and $\Delta\rho_{2\alpha/\beta}$, as shown in FIG. 5. Each contribution consists of two degenerate terms and the color code of the deformation density indicates the electron accumulation for blue and depletion for red.

For both spin channels, the bonding mechanisms are quite similar showing two significant components participating in the $Co\cdots B_{16}$ interactions. Taking the spin α as an example, the strongest contribution $\Delta E_{1\alpha}$ (-104.4 kcal/mol) comes from the bonding comprised of Co $d_{xy}/d_{x^2-y^2}$ and B_{16} $2e_2$ orbitals because of the more efficient orbital overlap (FIG. 4). The second strongest stabilization $\Delta E_{2\alpha}$ (-90.4 kcal/mol), constituting 20.2% contribution in total to the orbital interaction, arises from the interaction between Co d_{xz}/d_{yz} and B_{16} $2e_7$ orbitals. Thus, Co atom interacts with the surrounding B atoms dominantly through σ-type (d_{xy}, $d_{x^2-y^2}$) and π-type (d_{xz} and d_{yz}) interactions, while the d_{z^2} orbital was fully occupied ($5a_1$ in FIG. 4), contributing little to the $Co\cdots B_{16}$ interaction.

IV. CONCLUSION

A joint photoelectron spectroscopy and quantum chemistry study has been carried out to investigate the chemical bonding and electronic structure of CoB_{16}^-, the first metal-doped boron drum cluster. An improved photoelectron spectrum has been obtained, as well as more detailed electron structure calculations using the TDDFT approach combined with SAOP model to compute higher vertical detachment energies and simulate the full spectra commensurate with the experimental spectral range. Consistent with the previous study, isomers I (D_{8d}, $^3A_2$) and II (C_{4v}, $^1A_1$) are found to be close in energy and give rise to similar simulated spectra in agreement with the experimental data. The high stability of the drum structure is shown to originate from the strong interaction between Co and the B_{16} tube ligand via the Co $d_{xy}/d_{x^2-y^2}$ and d_{xz}/d_{yz} orbitals and the σ-type radial sp orbitals on B_{16}. Remarkably, the Co atom is found to have an unusually low oxidation state of -1 in the CoB_{16}^- anion through an inverted ligand field interaction between Co 3d and the B_{16} radial orbitals, whereas the neutral CoB_{16} can be viewed as a charge-transfer complex $Co^-@B_{16}^+$ with both covalent and ionic bonding.

V. ACKNOWLEDGEMENTS

The theoretical work done at Tsinghua University was supported by the National Natural Science Foundation of China (No.21590792, No.91426302, and No.21433005). The calculations were performed using resources from the Computational Chemistry Laboratory of the Department of Chemistry under the Tsinghua Xuetang Talents Program. The experimental work done at Brown University was supported by the U.S. National Science Foundation (CHE-1763380).

[1] J. Nagamatsu, N. Nakagawa, T. Muranaka, Y. Zenitani, and J. Akimitsu, Nature **410**, 63 (2001).
[2] H. Y. Chung, M. B. Weinberger, J. B. Levine, A. Kavner, J. M. Yang, S. H. Tolbert, and R. B. Kaner, Science **316**, 436 (2007).
[3] J. S. Kang, M. Li, H. Wu, H. Nguyen, and Y. Hu, Science **361**, 575 (2018).
[4] F. Tian, et al., Science **361**, 582 (2018).
[5] S. Li, Q. Zheng, Y. Lv, X. Liu, X. Wang, P. Y. Huang, D. G. Cahill, and B. Lv, Science **361**, 579 (2018).
[6] A. N. Alexandrova, A. I. Boldyrev, H. J. Zhai, and L. S. Wang, Coord. Chem. Rev. **250**, 2811 (2006).
[7] E. Oger, N. R. Crawford, R. Kelting, P. Weis, M. M. Kappes, and R. Ahlrichs, Angew. Chem. Int. Ed. **46**, 8503 (2007).
[8] A. P. Sergeeva, I. A. Popov, Z. A. Piazza, W. L. Li, C. Romanescu, L. S. Wang, and A. I. Boldyrev, Acc. Chem. Res. **47**, 1349 (2014).
[9] L. S. Wang, Int. Rev. Phys. Chem. **35**, 69 (2016).
[10] B. Kiran, S. Bulusu, H. J. Zhai, S. Yoo, X. C. Zeng, and L. S. Wang, Proc. Natl. Acad. Sci. USA **102**, 961 (2005).
[11] Z. A. Piazza, H. S. Hu, W. L. Li, Y. F. Zhao, J. Li, and L. S. Wang, Nat. Commun. **5**, 3113 (2014).
[12] H. J. Zhai, Y. F. Zhao, W. L. Li, Q. Chen, H. Bai, H. S. Hu, Z. A. Piazza, W. J. Tian, H. G. Lu, Y. B. Wu, Y. W. Mu, G. F. Wei, Z. P. Liu, J. Li, S. D. Li, and L. S. Wang, Nat. Chem. **6**, 727 (2014).
[13] W. L. Li, X. Chen, T. Jian, T. T. Chen, J. Li, and L. S. Wang, Nat. Rev. Chem. **1**, 0071 (2017).
[14] W. L. Li, H. S. Hu, Y. F. Zhao, X. Chen, T. T. Chen, T. Jian, L. S. Wang, and J. Li, Sci. Sin. Chim. **48**, 98 (2018).
[15] C. Romanescu, T. R. Galeev, A. P. Sergeeva, W. L. Li, L. S. Wang, and A. I. Boldyrev, J. Organomet. Chem. **721**, 148 (2012).
[16] C. Romanescu, T. R. Galeev, W. L. Li, A. I. Boldyrev, and L. S. Wang, Acc. Chem. Res. **46**, 350 (2012).
[17] T. R. Galeev, C. Romanescu, W. L. Li, L. S. Wang, and A. I. Boldyrev, Angew. Chem. Int. Ed. **51**, 2101 (2012).
[18] C. Romanescu, T. R. Galeev, W. L. Li, A. I. Boldyrev, and L. S. Wang, Angew. Chem. Int. Ed. **50**, 9334 (2011).
[19] W. L. Li, C. Romanescu, T. R. Galeev, Z. A. Piazza, A. I. Boldyrev, and L. S. Wang, J. Am. Chem. Soc. **134**, 165 (2011).
[20] I. A. Popov, W. L. Li, Z. A. Piazza, A. I. Boldyrev, and L. S. Wang, J. Phys. Chem. A **118**, 8098 (2014).
[21] I. A. Popov, T. Jian, G. V. Lopez, A. I. Boldyrev, and L. S. Wang, Nat. Commun. **6**, 8654 (2015).
[22] T. Jian, W. L. Li, X. Chen, T. T. Chen, G. V. Lopez, J. Li, and L. S. Wang, Chem. Sci. **7**, 7020 (2016).
[23] W. L. Li, T. Jian, X. Chen, T. T. Chen, G. V. Lopez, J. Li, and L. S. Wang, Angew. Chem. Int. Ed. **55**, 7358 (2016).

DOI:10.1063/1674-0068/cjcp1903050

[24] T. Jian, W. L. Li, I. A. Popov, G. V. Lopez, X. Chen, A. I. Boldyrev, J. Li, and L. S. Wang, J. Chem. Phys. **144**, 154310 (2016).
[25] W. L. Li, T. Jian, X. Chen, H. R. Li, T. T. Chen, X. M. Luo, S. D. Li, J. Li, and L. S. Wang, Chem. Commun. **53**, 1587 (2017).
[26] T. T. Chen, W. L. Li, T. Jian, X. Chen, J. Li, and L. S. Wang, Angew. Chem. Int. Ed. **56**, 6916 (2017).
[27] W. L. Li, T. T. Chen, D. H. Xing, X. Chen, J. Li, and L. S. Wang, Proc. Natl. Acad. Sci. USA **115**, E6972 (2018).
[28] T. T. Chen, W. L. Li, J. Li, and L. S. Wang, Chem. Sci. **10**, 2534 (2019).
[29] S. K. Ritter, Chem. Eng. News **93**, 27, (2015).
[30] L. S. Wang, H. S. Cheng, and J. Fan, J. Chem. Phys. **102**, 9480 (1995).
[31] K. Fehre, D. Trojanowskaja, J. Gatzke, M. Kunitski, F. Trinter, S. Zeller, L. P. H. Schmidt, J. Stohner, R. Berger, and A. Czasch, Rev. Sci. Instrum. **89**, 045112 (2018).
[32] Y. Zhao and D. G. Truhlar, Theor. Chem. Acc. **120**, 215 (2008).
[33] T. H. Dunning Jr., J. Chem. Phys. **90**, 1007 (1989).
[34] M. Dolg, U. Wedig, H. Stoll, and H. Preuss, J. Chem. Phys. **86**, 866 (1987).
[35] J. M. L. Martin and A. Sundermann, J. Chem. Phys. **114**, 3408 (2001).
[36] J. Li, X. Li, H. J. Zhai, and L. S. Wang, Science **299**, 864 (2003).
[37] O. V. Gritsenko, P. R. T. Schipper, and E. J. Baerends, Chem. Phys. Lett. **302**, 199 (1999).
[38] *ADF, 2016.101, SCM, Theoretical Chemistry*, Amsterdam, The Netherlands, Vrijie Universiteit, (http://www.scm.com).
[39] E. van Lenthe and E. J. Baerends, J. Comput. Chem. **24**, 1142 (2003).
[40] E. van Lenthe, E. J. Baerends, and J. G. Snijders, J. Chem. Phys. **99**, 4597 (1993).
[41] T. Ziegler and A. Rauk, Inorg. Chem. **18**, 1558 (1979).
[42] A. Michalak, M. Mitoraj, and T. Ziegler, J. Phys. Chem. A **112**, 1933 (2008).
[43] M. P. Mitoraj, A. Michalak, and T. Ziegler, J. Chem. Theory Comput. **5**, 962 (2009).
[44] J. P. Perdew, K. Burke, and M. Ernzerhof, Phys. Rev. Lett. **77**, 3865 (1996).
[45] R. Hoffmann, S. Alvarez, C. Mealli, A. Falceto, T. J. Cahill, T. Zeng, and G. Manca, Chem. Rev. **116**, 8173 (2016).
[46] R. S. Mulliken, J. Chem. Phys. **23**, 1833 (1955).
[47] M. Swart, P. T. v. Duijnen, and J. G. Snijders, J. Comput. Chem. **22**, 79 (2001).
[48] X. Chen, T. T. Chen, W. L. Li, J. B. Lu, L. J. Zhao, T. Jian, H. S. Hu, L. S. Wang, and J. Li, Inorg. Chem. **58**, 411 (2019).

DOI:10.1063/1674-0068/cjcp1903050